Phase separation in thermal systems: A lattice Boltzmann study and morphological characterization

Yanbiao Gan,[1,2,3] Aiguo Xu,[2,*] Guangcai Zhang,[2] Yingjun Li,[1,*] and Hua Li[2]

[1]*State Key Laboratory for GeoMechanics and Deep Underground Engineering, SMCE, China University of Mining and Technology (Beijing), Beijing 100083, P.R. China*

[2]*National Key Laboratory of Computational Physics, Institute of Applied Physics and Computational Mathematics, P.O. Box 8009-26, Beijing 100088, P.R. China*

[3]*North China Institute of Aerospace Engineering, Langfang 065000, P.R. China*

(Received 14 December 2010; revised manuscript received 11 September 2011; published 31 October 2011)

We investigate thermal and isothermal symmetric liquid-vapor separations via a fast Fourier transform thermal lattice Boltzmann (FFT-TLB) model. Structure factor, domain size, and Minkowski functionals are employed to characterize the density and velocity fields, as well as to understand the configurations and the kinetic processes. Compared with the isothermal phase separation, the freedom in temperature prolongs the spinodal decomposition (SD) stage and induces different rheological and morphological behaviors in the thermal system. After the transient procedure, both the thermal and isothermal separations show power-law scalings in domain growth, while the exponent for thermal system is lower than that for isothermal system. With respect to the density field, the isothermal system presents more likely bicontinuous configurations with narrower interfaces, while the thermal system presents more likely configurations with scattered bubbles. Heat creation, conduction, and lower interfacial stresses are the main reasons for the differences in thermal system. Different from the isothermal case, the release of latent heat causes the changing of local temperature, which results in new local mechanical balance. When the Prandtl number becomes smaller, the system approaches thermodynamical equilibrium much more quickly. The increasing of mean temperature makes the interfacial stress lower in the following way: $\sigma = \sigma_0[(T_c - T)/(T_c - T_0)]^{3/2}$, where T_c is the critical temperature and σ_0 is the interfacial stress at a reference temperature T_0, which is the main reason for the prolonged SD stage and the lower growth exponent in the thermal case. Besides thermodynamics, we probe how the local viscosities influence the morphology of the phase separating system. We find that, for both the isothermal and thermal cases, the growth exponents and local flow velocities are inversely proportional to the corresponding viscosities. Compared with the isothermal case, the local flow velocity depends not only on viscosity but also on temperature.

DOI: 10.1103/PhysRevE.84.046715 PACS number(s): 47.11.−j, 47.20.Hw, 05.70.Ln

I. INTRODUCTION

Multiphase flows and heat transfers are ubiquitous in nature, industrial processes, as well as daily life, e.g., oil-water systems, bubble flows, petroleum processing, paper making, and power plants [1]. Therefore, establishing accurate prediction models to investigate the underlying physical essence of these phenomena is of great academic significance and industrial practical value. However, due to the complex nature and inherent nonlinearities of multiphase flows, theoretical solutions are usually limited to a small class of problems in one dimension and with numerous simplifying assumptions and generalizations [2]. On the other hand, experimental approaches for multiphase flows are generally expensive and some problems are still being unsolved in accurate measurement technology (e.g., interfacial area measurement) for this process [3]. Consequently, it is reasonable to consider numerical simulation, to some extent, as a primarily useful tool in studying the underlying physics of multiphase flows and providing some insights into understanding the kinetic process, which are difficult to obtain from theoretical analysis or experiments.

Molecular dynamics (MD) is a nice microscopic approach, but it is too computationally expensive to access dynamic behaviors with spatiotemporal scales comparable with experiments [4]. Moreover, many macroscopic behaviors are, in fact, not sensitive to degrees of freedom at the molecular level. Traditional fluid dynamics does not work well for systems where nonequilibrium effects are pronounced, for example, multiphase system. In addition, from the computational expenses point of view, the direct simulation of fluid behaviors in such a system is also a challenging work, since it is not easy to track the deformable macroscopic interfaces and to incorporate the complex microscopic interactions [5].

Between these two approaches, as a mesoscopic approach, the lattice Boltzmann (LB) method has enjoyed substantial development and has become a very promising and versatile tool for simulating complex phenomena in various fields during the past two decades [6], ranging from magnetohydrodynamics [7,8], to compressible flows [9–12], wave propagations [13], hydrodynamic instabilities [14,15], etc. Apart from fields listed above, the versatile method is particularly promising in the area of multiphase systems [16–37]. This is mainly owing to its intrinsic kinetic nature, which makes the interparticle interactions (IPIs) be incorporated easily and flexibly and, in fact, the IPI is the underlying microscopic physical reason for phase separation and interfacial tension in multiphase systems. So far, many LB models for multiphase flows have been proposed, among which the three well-known ones are the Chromodynamic model by Gunstensen *et al.* [16], the pseudo-potential model by Shan and Chen [17,30], and the free energy model by Swift *et al.* [18].

*Corresponding authors: Xu_Aiguo@iapcm.ac.cn; lyj@aphy.iphy.ac.cn

The aforementioned models have been successfully applied to study a wide variety of multiphase flow problems in science and engineering, such as contact line motion [19,20], wetting [21], drop breakup [22,23], drop collision [24], chemically reactive fluid [25], phase separation and phase ordering [16–18,26–28,33,35–37], etc. Despite this, to date, most studies focus on the isothermal systems (except for models reported in Refs. [36,37]), because, in these models, only mass and momentum conservations are kept; hydrodynamic behaviors due to temperature field are not taken into account. However, thermal effects are significant, even dominant, in many cases. Examples include phase separations in the boiling process, distillation and condensation processes, thermal nuclear reactors, etc. In these systems, the evolutions of the temperature and flow fields are spontaneously coupled with each other [38,39]. Therefore, it is a fundamental and essential work to develop thermal LB (TLB) models for multiphase system. But due to the complexity of this problem, the progress has been rather slow.

The most obvious obstacle lies in the fact that, when the interparticle forces are incorporated, how to ensure the total energy conservation becomes challenging in the discrete model. To overcome this difficulty, extensive efforts have been made over the past few years. But until very recently, only a few TLB models for multiphase flows have been proposed and can be roughly divided into two approaches. The first is the passive scalar approach [40,41]. In this approach, evolutions of the density field and the momentum field are solved by an isothermal LB model, while the evolution of temperature is determined by an additional passive scalar equation. The coupling of these two parts is through a suitably defined body force in the isotherm LB equation. This approach is conceptually rather simple and as stable as the isothermal LB models, because the energy conservation is not explicitly implemented. Meanwhile, it can recover an equation of state (EOS) for nonideal gas and capture the temperature field. However, it should be pointed out that, in the passive scalar approach, the viscous dissipation and compression work done by the pressure are neglected [41].

The second is the multispeed approach, which implements energy conservation by using larger and more isotropic sets of velocities and by including higher-order velocity terms in the equilibrium distribution. Examples of an ideal gas include the works of Alexander *et al.* [42], Watari *et al.* [9], Xu *et al.* [10,15], and others. However, applications of this approach to thermal flows with high Mach number or flows with high Knudsen number still have some challenges. The challenges arise from the insufficient truncation in the equilibrium distribution function and the insufficient isotropy in the discrete-velocity model (DVM). In an alternative way, using the Hermite expansion approach, Shan *et al.* [43] presented a systematic theoretical framework for constructing TLB models that approximate the continuum Boltzmann equation with higher accuracy. With the Hermite expansion approach, hydrodynamic moments at various levels can be determined in a straightforward way at a given order of truncations of the Hermite polynomials. Almost simultaneously, similar results were obtained by Philippi *et al.* [44] using a different procedure. Although the above-mentioned TLB models work only for ideal gas systems, they can be extended to multiphase flows by the extra force method. The one developed by Gonnella, Lamura, and Sofonea (GLS) [45] is typical. In this model, an extra term I_{ki}, accounting for interparticle forces, is added into the LB equation to describe the van der Waals (VDW) fluids. From the IPI point of view, it can be considered as a bottom-up approach, similar to the Shan-Chen model. To describe system with interfaces, gradient contributions to free energy due to the inhomogeneity of fluid density are also included. Compared with the passive scalar approach, all observable fields, e.g., density, velocity, temperature, and pressure, are directly derived from the same distribution function, as in the standard kinetic theory.

In a recent work [46], we further develop the GLS model so that the total energy conservation can be better held and the spurious velocities can be damped to negligible scale in numerical simulations. In the improved model, spatial derivatives in the convection term and the force term are calculated via the fast Fourier transform (FFT) and its inverse (IFFT). For convenience of description, we refer to this model as the FFT-TLB model. Via the FFT-TLB model, we study the effects of temperature and viscosity on liquid-vapor phase separation in the two-dimensional case. It is known that spatial domains of homogeneous phases evolving during spinodal decomposition (SD) show a large variety of complex spatial patterns, and the system is globally in a nonequilibrium state. How to effectively describe and pick up information from such a complex system is still an open problem. In the present work, besides the rheological behavior, we use the Minkowski functionals [47] to characterize the isothermal and thermal phase separations and conduct a comparison study on the similarities and differences between these two cases.

The following parts of the paper are planned as follows. The Minkowski functionals and the FFT-TLB model are briefly reviewed in Secs. II and III, respectively. Simulation results and corresponding physical interpretations are given in Sec. IV. Section V presents conclusions and discussions.

II. MORPHOLOGICAL CHARACTERIZATION

In this section we briefly review the set of statistics known as Minkowski functionals [47], which will be used to characterize the physical fields in Sec. IV. Such a description has been well known in digital picture analysis [48] and successfully adapted to characterize the reaction-diffusion systems [49], shocked porous materials [50], and patterns in phase separation of complex fluids [27,51,52], etc.

According to a general theorem of integral geometry, all properties of a d-dimensional convex set, which satisfy motion invariance and additivity, are contained in $d+1$ numerical values [53]. For a pixelized map $\psi(\mathbf{x})$, we consider the excursion sets of the map, defined as the set of all map pixels with value of ψ greater than some threshold ψ_{th}, where $\mathbf{x}$ is the position, ψ can be a state variable such as density ρ, temperature T, or pressure P; ψ can also be the velocity $\mathbf{u}$ or its components, or some specific stress, etc. Then the $d+1$ functionals of these excursion sets completely describe the morphological properties of the underlying map $\psi(\mathbf{x})$. In the case of two- or three-dimensions, the Minkowski functionals have intuitive geometric interpretations. For a two-dimensional density map $\rho(\mathbf{x})$, the three Minkowski

functionals correspond geometrically to the fractional area A of the high-density domains, the boundary length L between the the high- and low-density domains, and the Euler characteristic χ.

In this work we probe the effects of temperature and viscosity on phase separation by checking the density map $\rho(\mathbf{x},t)$ and velocity map $\mathbf{u}(\mathbf{x},t)$, where time t is explicitly denoted. When the density $\rho(\mathbf{x},t)$ is beyond the threshold value ρ_{th}, the grid node at position $\mathbf{x}$ is regarded as a white vertex; otherwise it is regarded as a black one. For the square lattice, a pixel possesses four vertices. A region with connected white (black) pixels is defined as a white (black) domain. Two neighboring white and black domains present an interface or boundary. When the threshold contour level ρ_{th} increases from the lowest density $\rho_{\min}$ to the highest one $\rho_{\max}$, the white area fraction $A = N_A^w/N$ will decrease from 1 to 0, and the qualitative features of the patterns will vary drastically, where N_A^w is the number of pixels with a density larger than ρ_{th}, $N = N_x \times N_y$ is the total number of pixels, N_x and N_y are the lattice numbers along the x and y directions, respectively; the boundary length $L = N_L/N$ is defined as the ratio between the pixels separating the black and white domains, and the total number of pixels. With the increasing of ρ_{th}, boundary length L first increases from 0 at $\rho_{\text{th}} = \rho_{\min}$, then arrives at a maximum value $L_{\max}$, and finally decreases to 0 again at $\rho_{\text{th}} = \rho_{\max}$; the third morphological quantity is the Euler characteristic χ, defined as the difference of the number of connected white domains N_χ^w and black domains N_χ^b normalized by N, $\chi = (N_\chi^w - N_\chi^b)/N$. In contrast to the white area A and boundary length L, the Euler characteristic χ describes the connectivity of the domains in a purely topological way. It is negative (positive) if many disconnected black (white) regions dominate the image. A vanishing Euler characteristic indicates a highly connected structure with equal numbers of black and white domains. Despite having global meaning, the Euler characteristic χ can be calculated in a local way using the additivity relation [27,49,52]. Since the measures are normalized by N, they can be used to compare systems with different sizes.

III. FFT-TLB MULTIPHASE MODEL

In this section we present the FFT-TLB model for simulating a thermal liquid-vapor system. The model is a further development of the one proposed by GLS [45]. GLS introduced an appropriate interparticle force term to describe the VDW fluids. Our contribution is to propose an appropriate FFT scheme, which is used to calculate the convection term and the force term. With this new model, the nonconservation problem of total energy due to spatiotemporal discretizations is much better solved, and spurious currents in equilibrium interfaces are significantly reduced in the numerical simulations.

A. TLB multiphase model by GLS

The GLS model includes the following two parts: (1) TLB model by Watari-Tsutahara (WT) [9] and (2) an appropriate interparticle force, I_{ki}. The original WT model works only for ideal gas. It uses the following DVM:

$$\mathbf{v}_0 = 0, \quad \mathbf{v}_{\text{ki}} = v_k\left[\cos\left(\frac{i-1}{4}\pi\right), \sin\left(\frac{i-1}{4}\pi\right)\right], \quad k = 1,2,3,4; \quad i = 1,2,\ldots,8, \tag{1}$$

where subscript k indicates the kth group of particle velocities whose speed is v_k and i represents the direction of particle's speed. Different from the standard LB model, the WT model uses a second upwind finite-difference (FD) scheme to calculate the convection term in the LB equation. The FD LB model breaks the combination of discretizations of space and time, which makes the particle speeds more flexible. The values of the speeds $\mathbf{v}_k$ may be determined in such a way that the temperature gets a large interval around the critical temperature T_c, under which the simulation is stable. This is of great importance for phase separation studies where long-lasting simulations are needed to determine the growth behavior [26].

Compared to WT model, the main contribution of GLS model is the introduction of the extra term I_{ki}, which accounts for interparticle forces

$$\frac{\partial f_{\text{ki}}}{\partial t} + \mathbf{v}_{\text{ki}} \cdot \frac{\partial f_{\text{ki}}}{\partial \mathbf{r}} = -\frac{1}{\tau}\left[f_{\text{ki}} - f_{\text{ki}}^{\text{eq}}\right] + I_{\text{ki}}, \tag{2}$$

where $f_{\text{ki}}^{\text{eq}}$ is the local equilibrium distribution function, $\mathbf{r}$ the spatial coordinate, and τ the relaxation time related to the kinematic viscosity. The distribution function $f_{\text{ki}}^{\text{eq}}$ is related to the local density ρ, fluid velocity $\mathbf{u}$, and temperature T through the following moments:

$$\rho = \sum_{\text{ki}} f_{\text{ki}}^{\text{eq}}, \tag{3}$$

$$\rho\mathbf{u} = \sum_{\text{ki}} \mathbf{v}_{\text{ki}} f_{\text{ki}}^{\text{eq}}, \tag{4}$$

$$\rho T = \sum_{\text{ki}} \frac{1}{2}(\mathbf{v}_{\text{ki}} - \mathbf{u})^2 f_{\text{ki}}^{\text{eq}}. \tag{5}$$

I_{ki} in Eq. (2) takes the following form:

$$I_{\text{ki}} = -[A + B_\alpha(v_{\text{ki}\alpha} - u_\alpha) + (C + C_q)(v_{\text{ki}\alpha} - u_\alpha)^2] f_{\text{ki}}^{\text{eq}}, \tag{6}$$

with

$$A = -2(C + C_q)T, \tag{7}$$

$$B_\alpha = \frac{1}{\rho T}[\partial_\alpha(P^w - \rho T) + \partial_\beta \Lambda_{\alpha\beta} - \partial_\alpha(\zeta\,\partial_\gamma u_\gamma)], \tag{8}$$

$$C = \frac{1}{2\rho T^2}\Big\{(P^w - \rho T)\partial_\gamma u_\gamma + \Lambda_{\alpha\beta}\partial_\alpha u_\beta - (\zeta\,\partial_\gamma u_\gamma)\partial_\alpha u_\alpha + \frac{9}{8}\rho^2\partial_\gamma u_\gamma + K\Big[-\frac{1}{2}(\partial_\gamma\rho)(\partial_\gamma\rho)(\partial_\alpha u_\alpha) - \rho(\partial_\gamma\rho)(\partial_\gamma\partial_\alpha u_\alpha) - (\partial_\gamma\rho)(\partial_\gamma u_\alpha)(\partial_\alpha\rho)\Big]\Big\}, \tag{9}$$

$$C_q = \frac{1}{2\rho T^2}\partial_\alpha[2q\rho T(\partial_\alpha T)]. \tag{10}$$

$P^w = 3\rho T/(3-\rho) - 9\rho^2/8$ is the VDW EOS. Since the pressure is not monotonic in density, the thermodynamic phase

transition may occur in such a system. By setting $\partial P^w/\partial\rho = 0$, $\partial^2 P^w/\partial\rho^2 = 0$, we obtain the critical point $T_c = \rho_c = 1$. $\Lambda_{\alpha\beta} = M\partial_\alpha\rho\partial_\beta\rho - [\rho T\partial_\gamma\rho\partial_\gamma(M/T)]\delta_{\alpha\beta} - M(\rho\nabla^2\rho + |\nabla\rho|^2/2)\delta_{\alpha\beta}$ is the contribution of density gradient to pressure tensor and $M = K + HT$ allows a dependence of the surface tension on temperature, where K is the surface tension coefficient and H is a constant. It is noteworthy to point out that, in this model, the Prandtl number $\mathrm{Pr} = \eta/\kappa_T = \tau/2(\tau - q)$ can be changed by adjusting the parameter q in the term C_q.

It has been shown that [45], under the Chapman-Enskog expansion, the above LB model recovers the following equations for VDW fluids:

$$\partial_t\rho + \partial_\alpha(\rho u_\alpha) = 0, \tag{11}$$

$$\partial_t(\rho u_\alpha) + \partial_\beta(\rho u_\alpha u_\beta + \Pi_{\alpha\beta} - \sigma_{\alpha\beta}) = 0, \tag{12}$$

$$\partial_t e_{\mathrm{tot}} + \partial_\alpha[e_{\mathrm{tot}}u_\alpha + (\Pi_{\alpha\beta} - \sigma_{\alpha\beta})u_\beta - \kappa_T\partial_\alpha T] = 0, \tag{13}$$

where $\Pi_{\alpha\beta} = P^w\delta_{\alpha\beta} + \Lambda_{\alpha\beta}$ is the nonviscous stress, and $\sigma_{\alpha\beta} = \eta(\partial_\alpha u_\beta + \partial_\beta u_\alpha - \partial_\gamma u_\gamma\delta_{\alpha\beta}) + \zeta\partial_\gamma u_\gamma\delta_{\alpha\beta}$ is the dissipative tensor with the shear and bulk viscosities η and ζ. $e_{\mathrm{tot}} = \rho T - 9\rho^2/8 + K|\nabla\rho|^2/2 + \rho u^2/2$ is the total energy density. It should be mentioned that the force term also accounts for the potential energy $-9/8\rho^2$ and interfacial energy $K|\nabla\rho|^2/2$, which are sources of the macroscopic kinetic energy and the thermal energy.

B. Our contribution: Spatial discretization with FFT

In this subsection, we will review our improvements to the TLB multiphase model: spatial derivatives in the convection term $\mathbf{v}_{\mathrm{ki}}\cdot\partial f_{\mathrm{ki}}/\partial\mathbf{r}$ and in the external force term I_{ki} are calculated via the FFT scheme and its inverse.

To illustrate the necessity, we present simulation results for a thermal phase separation process by various numerical schemes. Here the time derivative is calculated using the first-order forward Euler FD scheme. Spatial derivatives in I_{ki} are calculated using the second-order central difference (second CD) scheme. Spatial derivatives in convection term $\mathbf{v}_{\mathrm{ki}}\cdot\partial f_{\mathrm{ki}}/\partial\mathbf{r}$ are calculated using the the second CD scheme, the Lax-Wendroff (LW) scheme, the nonoscillatory and nonfree-parameter dissipation (NND) scheme [54], and the fifth-order weighted essentially nonoscillatory scheme (5th WENO) [55], respectively. As a result, we find that the total energy density $e_{\mathrm{tot}}(t)$ is not conservative in simulations, even though it is in theoretical analysis (see Fig. 1). The nonconservation of energy is caused by errors of spatiotemporal discretizations.

Aiming to solve the problem of energy nonconversation, we proposed a new algorithm based on FFT and its inverse [46]. This approach is especially powerful for a periodic system and also provides spatial spectral information on field quantities. For completeness, let us start with the definition of Fourier transform of a discrete function $f(x_j)$:

$$\widetilde{f}(k) = \Delta x\sum_{j=0}^{N-1} f(x_j)e^{-ikx_j}, \tag{14}$$

and its inverse

$$f(x_j) = \frac{1}{L}\sum_{n=-N/2}^{N/2-1}\widetilde{f}(k)e^{ikx_j}, \tag{15}$$

where i is an imaginary unit, $k = 2\pi n/L$ and $L = N\Delta x$ is the length of the system divided into N equal segments. A general theorem of derivative based on FFT states that [56–58]

$$\widetilde{f}'(k) = ik\times\widetilde{f}(k), \tag{16}$$

where $\widetilde{f}'(k)$ is the Fourier transform of $f'(x_j)$, k is the module of wave vector $\mathbf{k}$. The theorem provides a way to calculate the spatial derivative $f'(x_j)$, composed of the following steps: (1) Transform $f(x_j)$ in real space into $\widetilde{f}(k)$ in reciprocal space; (2) multiply $\widetilde{f}(k)$ with ik; (3) take the inverse Fourier transform (IFT) of $\widetilde{f}'(k)$, and then the spatial derivative $f'(x_j)$ can be obtained. A higher-order derivative, such as the nth derivative $f^{(n)}(x_j)$ $(n\geqslant 2)$, can be obtained from a similar procedure only if we multiply $\widetilde{f}(k)$ with $(ik)^n$,

$$\widetilde{f^{(n)}}(k) = (ik)^n\times\widetilde{f}(k). \tag{17}$$

High-order derivatives that can be calculated from this convenient way is a main merit of FFT over FD scheme; otherwise, we should choose more stencils (more points) to approximate high-order derivatives.

The FFT approach has excellent accuracy properties, typically well beyond that of standard discretization schemes. In principle, it gives the exact derivative with infinite order accuracy if the function is infinitely differentiable [57–60]. In our manuscript, using this virtue, the FFT scheme is designed to approximate the true spatial derivatives, as a result, to eliminate spurious velocities near the interface region and to guarantee energy conservation. However, the trouble in proceeding in this manner is that, in many cases, it is difficult to ensure that the infinite differentiability condition is satisfied. For example, the function $f'(x_j)$ may have a discontinuity of the same character as the square wave. Then the discontinuity will induce oscillations, known as the Gibbs phenomenon. The Gibbs phenomenon influences the accuracy of the FFT not only in the neighborhood of the point of singularity, but also over the entire computational domain. Since the Gibbs phenomenon is related to the slow decay of the Fourier coefficients of the discontinuous function, it is natural to use smoothing procedures, which attenuate higher-order Fourier coefficients to damp the oscillations [57,59,61,62]. A straightforward way is to multiply each Fourier coefficients by a smoothing factor σ_k, for instance, the Lanczons smoothing factor, the raised cosine smoothing factor, or the Fejer smoothing factor, etc. [57,61,62].

In the recent work [46], we presented a way to construct smoothing factors. First, we expand k in Taylor series:

$$k = \frac{\arcsin[\sin(k\Delta x/2)]}{\Delta x/2} = \frac{1}{\Delta x/2}\left[\sin(k\Delta x/2) + \frac{1}{6}\sin^3(k\Delta x/2)\right.$$

$$+\frac{3}{40}\sin^5(k\Delta x/2)+\frac{5}{112}\sin^7(k\Delta x/2)+\cdots\Big]$$
$$=\frac{1}{\Delta x/2}\sum_{n=0}^{\infty}\frac{\Gamma(n/2)\delta_{0,\Theta(n)}\varepsilon(-1+n)}{\sqrt{\pi}n\Gamma\left(\frac{n+1}{2}\right)}\sin^n(k\Delta x/2), \quad (18)$$

where $\Gamma(n)=\int_0^\infty t^{n-1}e^{-t}\,dt$ is the Gamma function, $\Theta(n)=\mathrm{Mod}[-1+n,2]$ is the Mod function, and $\varepsilon(-1+n)$ is the unit step function. Next, in order to refrain the Gibbs oscillation, we should filter out more high-frequency waves, or at least damp the strengths of high-frequency waves. Therefore, k may take the form of an appropriately truncated Taylor series expansion of $\sin(k\Delta x/2)$. For example, k can take the following forms:

$$k_1=\frac{\sin(k\Delta x/2)}{\Delta x/2}, \quad (19)$$

$$k_2=k_1+\frac{\sin^3(k\Delta x/2)/6}{\Delta x/2}, \quad (20)$$

$$k_3=k_2+\frac{3\sin^5(k\Delta x/2)/40}{\Delta x/2}, \quad (21)$$

and

$$k_4=k_3+\frac{5\sin^7(k\Delta x/2)/112}{\Delta x/2}, \quad (22)$$

then the calculated spatial derivative is second-order, fourth-order, sixth-order, and eighth-order in precision, respectively. Moreover, it is found that k_1 is consistent with the one used in Ref. [63]. Finally, the smoothing factor for k_1 can be expressed as

$$\sigma_1=\frac{k_1}{k}=\frac{\sin(j\pi/N_x)}{j\pi/N_x},\ j=-N_x/2,\ldots,N_x/2, \quad (23)$$

and the ones for k_2, k_3, and k_4 can be formulated in a similar way.

As reported in our recent work [46], the lower-order smoothing factors, such as σ_1 and σ_2, are much more effective to damp the strengthens of high-frequency waves and may result in excessively smeared approximations, which are unfaithful representations of the true physics. On the other hand, the higher-order smoothing factors, such as σ_3 and σ_4, can reserve more higher-frequency waves but may not damp the Gibbs phenomenon when the discontinuities are strong enough, and then cause numerical instability. This is especially true for the case with shock waves and/or discontinuities. The smoothing factors should survive the dilemma of stability versus accuracy. In other words, they should be minimal but make the evolution stable. In the present study, we focus on the liquid-vapor system without shock waves and strong discontinuities. Therefore, the FFT scheme with higher-order smoothing factor σ_4 is used throughout our simulations.

For comparisons, we verify the proposed FFT algorithm with the same problem described in Fig. 1 and display variations of density $\Delta\rho(t)$, momentum $\Delta(\rho\mathbf{u})(t)$, and total energy density $\Delta e_{\mathrm{tot}}(t)$ in Fig. 2, respectively. It is observed that, when the FFT scheme with σ_4 is adopted, variations of density and momentum nearly decrease to machine accuracy. For $\Delta e_{\mathrm{tot}}(t)$, it oscillates at the beginning and then goes to nearly a constant. Behaviors of $\Delta e_{\mathrm{tot}}(t)$ can be interpreted as follows. At the beginning of phase separation, the fluids

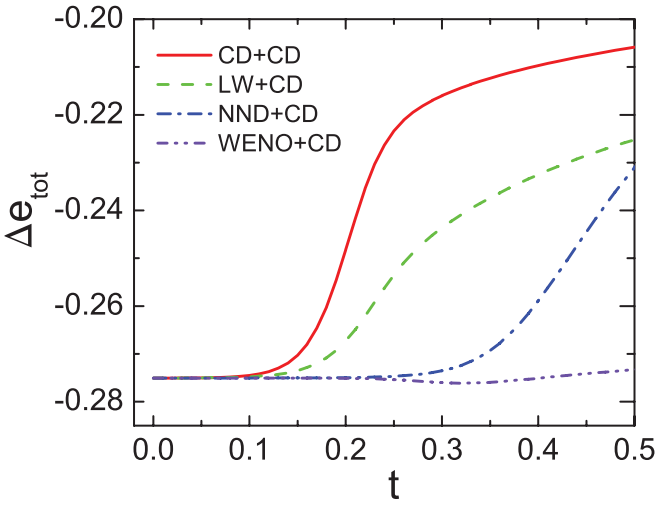

FIG. 1. (Color online) Variations of the total energy density $\Delta e_{\mathrm{tot}}(t)=e_{\mathrm{tot}}(t)-e_{\mathrm{tot}}(0)$ for a phase-separating system obtained from the GLS model with various schemes. Initial conditions are set as $\rho=1+\Delta$, $T=0.85$, $u_x=u_y=0$, where Δ is a random density with an amplitude of 0.01. The remaining parameters are as follows: $v_1=1.00$, $v_2=1.90$, $v_3=2.90$, $v_4=4.30$, $\tau=10^{-2}$, $\Delta x=\Delta y=1/256$, $\Delta t=10^{-5}$, $K=5\times10^{-6}$, $H=0$, $\zeta=0$, $q=-0.004$. Periodical boundary conditions (PBCs) are imposed on both the x and y directions.

spontaneously separate into small regions with higher and lower densities, and more liquid-vapor interfaces appear. Subsequently, spatial discretization errors induced by the interfaces (density gradients) arrive at their maxima, accounting for the initial oscillations. As time evolves further, under the action of surface tension, the total liquid-vapor interface length decreases owing to the coalescence of small domains, and then the discretization errors together with the amplitude of $\Delta e_{\mathrm{tot}}(t)$ decrease.

After about 10^6 time steps, the maximum derivation of e_{tot} is only about 1.5×10^{-7}, indicating that the FFT scheme has more advantage to guarantee energy conservation. Furthermore, we find that $\Delta e_{\mathrm{tot}}(t)$ decreases with decreasing the initial random density Δ. When Δ decreases to 0.001, the maximum of $\Delta e_{\mathrm{tot}}(t)$ will further decreases to 3×10^{-8} (not

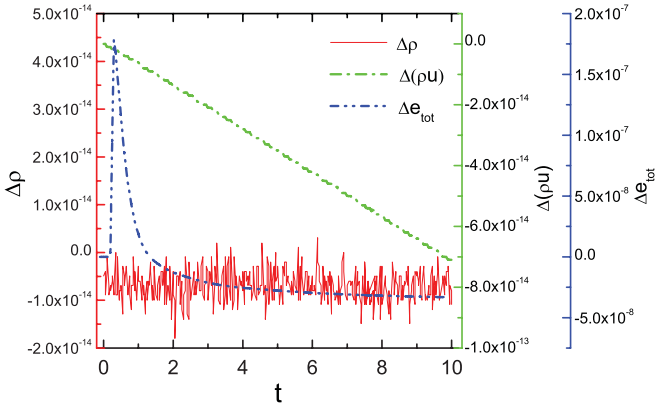

FIG. 2. (Color online) Variations of density $\Delta\rho(t)$, momentum $\Delta(\rho\mathbf{u})(t)$, and total energy $\Delta e_{\mathrm{tot}}(t)$ for the phase-separating system described in Fig. 1.

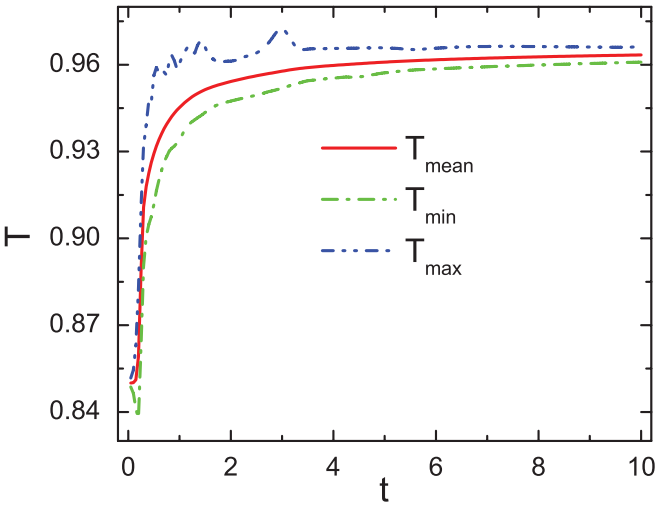

FIG. 3. (Color online) Temperatures versus time t for the FFT-TLB scheme.

shown here). Numerically, this is owing to the smaller density gradients in the interface regions as Δ decreases that reduce the spatial discretization errors. Actually, $\Delta = 0.001$ (0.1% of the initial density) is enough to generate phase separation and is more appropriate [28]. When Δ is larger, or the initial temperature is far below the critical one, the initial state of the system is very far from the equilibrium, and we may encounter large values of the fluid velocity in the early stage of simulation. Since the initial values of the velocity is zero everywhere, this process is responsible for a strong decrease in the local temperature (see Fig. 3).

Another interesting phenomenon is illustrated in Fig. 3. The mean and maximum temperatures rise sharply at the initial period of phase separation, while the minimum one decreases significantly at first and rises rapidly at later times. The difference between the minimum and the maximum ones $\Delta T = T_{\max} - T_{\min}$ arrives at its maximum at about $t = 0.25$. After that, ΔT decreases with time and goes to a constant value (nearly vanishing) when $t > 8$. The reasons for behaviors of temperatures are that: At the initial stage, the potential energy $-9/8\rho^2$, a part of the free energy, is high, so the system will relax. During phase separation, part of the potential energy transforms into the thermal energy ρT; namely, latent heat is locally released and conducts to the entire region. This is the main reason why temperatures are rising during simulations and the main difference from the isothermal case, where latent heat is extracted from the system by fixing the temperature in all lattice nodes. In addition, viscous dissipation is another mechanism of heat generation. More preciously, heat is created locally due to the fraction between fluid flows with different velocities. After phase separation, interfaces form and the fluid velocities go to zero everywhere. Then the macroscopic kinetic energy transforms into thermal energy totally.

In our recent work, the FFT-TLB multiphase model has been validated successfully by two sets of typical benchmarks [46]. Simulation results demonstrate that the FFT-TLB model can capture both qualitatively and quantitatively the interface properties in accord with the VDW theory. In addition, with the new model, spurious velocities near the liquid-vapor interface are significantly reduced, and, as a result, phase diagrams of the liquid-vapor system obtained from simulations are more consistent with that from theoretical calculations.

IV. SIMULATION RESULTS, RHEOLOGICAL AND MORPHOLOGICAL CHARACTERIZATIONS

When a system is suddenly quenched into the two-phase region, the original single phase becomes unstable, and then phase separation occurs through the formation and the subsequent growth of domains. Eventually, the system arrives at a new equilibrium state. In the past few decades, this phenomenon has been extensively studied [6,17,18,26–28,36–39,64–73], by theoretical derivations, experiments, and numerical simulations. Among others, the most significant finding is the domain growth law, which states that, at late times, the characteristic domain size $R(t)$ grows as a power with time t, $R(t) \sim t^{\alpha}$. The value of exponent α is believed to be universal, depending only on the growth mechanism, and has been well known in isothermal system, $\alpha = 1/2$ and $2/3$ for higher and lower viscosities, respectively [28,65,66,69,71]. However, behaviors of phase separation with temperature field are far from clear. The aim of this section is to clarify effects of temperature dynamics on both the rheological and morphological behaviors of phase separation.

A. Patterns for isothermal and thermal cases

Simulations for isothermal and thermal phase separations are performed on lattices with $N_x \times N_y = 512 \times 512$ nodes. PBCs are imposed on both two directions. Here we consider only symmetric mixtures; namely, we set liquid:vapor mass fractions to 1:1, for which at late times these domains will form a bicontinuous structure with sharp interfaces in the isothermal case [72,73]. Therefore, the initial conditions are set as follows:

$$(\rho, u_x, u_y, T) = (1.042 + \Delta, 0.0, 0.0, 0.9), \qquad (24)$$

where 1.042 is the mean density of liquid and vapor at $T = 0.9$, and Δ is a random density noise with an amplitude of 0.001. Parameters are set to be $\tau = 10^{-3}$, $\Delta t = 10^{-5}$, $K = 5 \times 10^{-6}$, $\Delta x = \Delta y = 1/256$, and others are unchanged. Density distribution patterns at representative times $t = 0.4$, 1.0, 2.5, and 8.0 are shown in Fig. 4 for the isothermal case [see Figs. 4I(a)–I(d)] and thermal case [see Figs. 4II(a)–II(d)]. For the isothermal case, after about 25 000 time steps, the fluid has begun to separate spontaneously into small regions with higher and lower densities. As time evolves, small domains merge with each other and larger domains appear under the action of surface tension at $t = 0.4$. From patterns at $t = 0.4$, 1.0, and 2.5, as excepted, higher and lower densities domains evolve in an equal way, leading to an interwoven bicontinuous pattern. The growth of domains continues at $t = 8.0$, and, eventually, the system will reach a completely separated state for a large enough time.

Compared with configurations in the isothermal case, several distinctive differences can be found in the thermal case: (1) The average size of domains in each case tends to increase

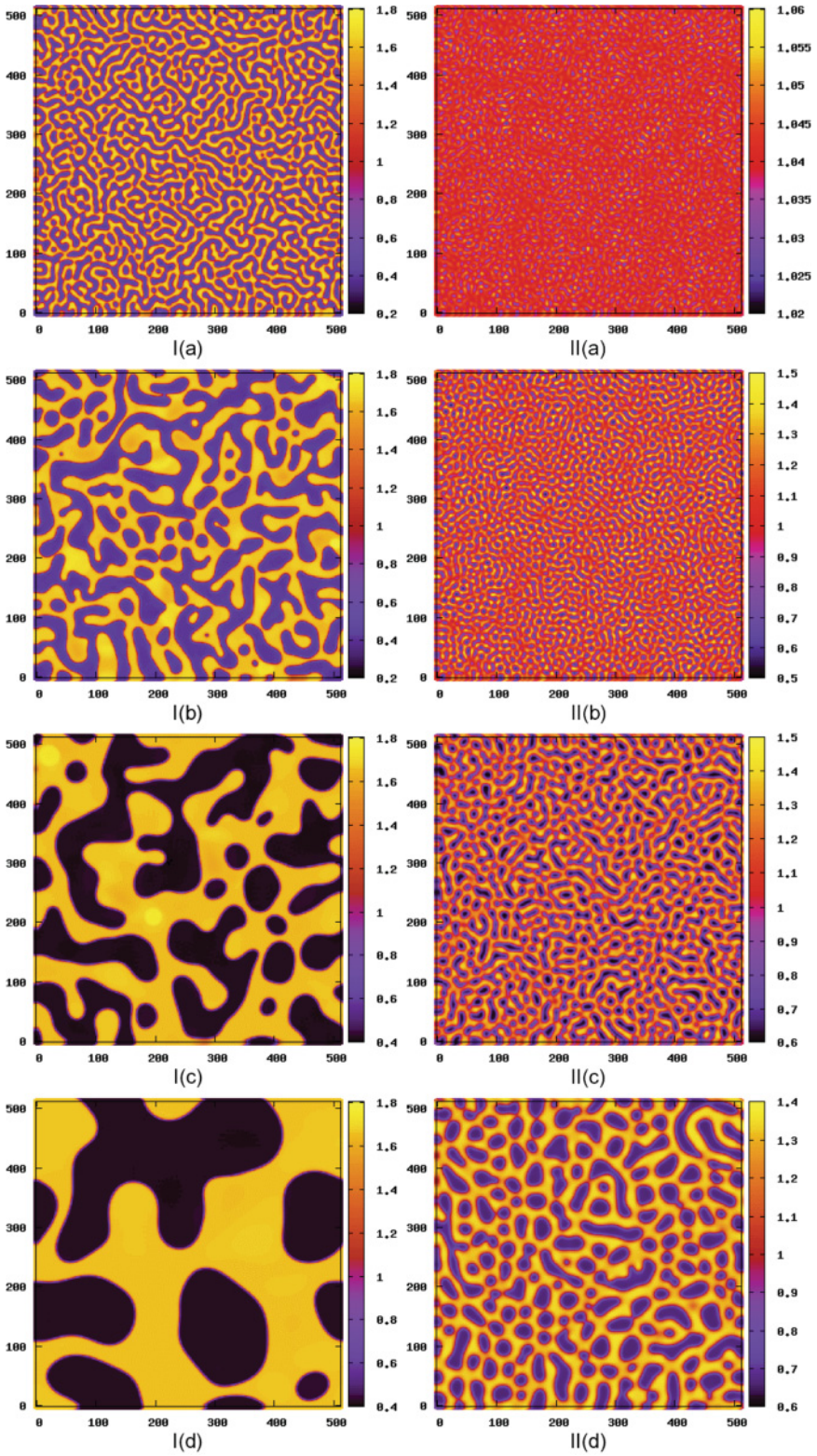

FIG. 4. (Color online) Snapshots in two processes of phase separations. The temperature is fixed at $T = 0.9$ in process I. See panels I(a)–I(d). The initial temperature in process II is $T = 0.9$. See panels II(a)–II(d). The relaxation time is fixed at $\tau = 10^{-3}$ in the two processes. The time $t = 0.4$, 1.0, 2.5, and 8.0 in panels (a), (b), (c), and (d), respectively. The lattice size here is 512×512.

in an effort to decrease the interfacial energy, while at the same moment, in the isothermal case, it is bigger than its counterpart, which demonstrates that domains grow faster in this case; (2) for the isothermal case, interfaces between vapor and liquid are much clearer, which indicates that the liquid-vapor interfaces in this case are much narrower; (3) the density difference between the maximum and minimum densities $\Delta\rho = \rho_{\max} - \rho_{\min}$ in the isothermal case is much larger than the one in the thermal case, showing that the phase separation in this case is deeper; (4) contrary to interpenetrating bicontinuous structures formed in the isothermal case, isolated and nearly circle vapor droplets suspending in the liquid phase appear in the thermal case. These differences are interesting and meaningful. In the following subsections, we will analyze these differences with the help of rheological description and Minkowski functionals.

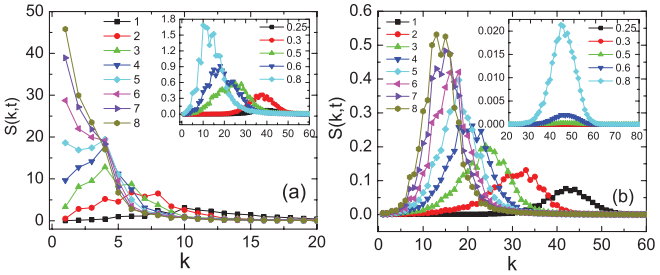

FIG. 5. (Color online) Spherically averaged structure factor $S(k,t)$ versus wave number k for the procedures shown in Fig. 4. Panel (a) is for the isothermal case, and panel (b) is for the thermal case. In each figure, $S(k,t)$ at times $t = 0.25$, 0.3, 0.5, 0.6, and 0.8 are shown in the inset, while those at times $t = 1.0$, 2.0, 3.0, 4.0, 5.0, 6.0, 7.0, and 8.0 are shown in the main frame.

B. Rheological characterization

In order to further quantify the results shown in Fig. 4, time evolution of the circularly averaged structure factor $S(k,t)$ is employed, which is defined as the Fourier transform of the density-density correlation function. For a discrete system, it can be stated as

$$S(\mathbf{k},t) = \left| \sum_{\mathbf{x}} [\rho(\mathbf{x},t) - \bar{\rho}(t)] e^{i\mathbf{k}\cdot\mathbf{x}} \right| / N, \tag{25}$$

where $\mathbf{k} = (2\pi/N)(m\hat{i} + n\hat{j})$ is the wave vector in the reciprocal space with $m = 1,2,\ldots,N_x$, $n = 1,2,\ldots,N_y$. $S(\mathbf{k},t)$ is further smoothed by averaging over an entire shell in $\mathbf{k}$ space to obtain the circularly averaged structure factor:

$$S(k,t) = \sum_{k} S(\mathbf{k},t) \Big/ \sum_{k} 1. \tag{26}$$

In Fig. 5 we present the time evolution of $S(k,t)$ for the isothermal case in panel (a) and thermal case in panel (b), respectively. All curves in Fig. 5 can be roughly divided into two different time regimes: the SD stage and the domain growth (DG) stage. From Fig. 5(a), at early times, such as $t = 0.25$ and 0.3, we observe that the peak in $S(k,t)$ increases in height without the position of the peak changing in time. This behavior is indicative of the initial sharpening of domains, without detectable phase separation taking place. In the second stage, the peak of $S(k,t)$ increases in height and shifts to smaller wave number, indicating the coarsening of domains. At $t = 0.5$, 0.6, and 0.8, we observe the appearance of a second peak in $S(k,t)$, which merges with the main peak later. This behavior manifests that there is more than one typical domain size at that moment. From $t = 6.0$ onward, the peak seems to stop drifting to the left but only oscillates in amplitude, demonstrating that the finite size effects are pronounced.

Similar results can also be found in the thermal case. Nevertheless, careful comparisons of these two cases will show you some distinctions: (1) The first stage continues up to $t = 0.8$, which is longer than that in the isothermal case. The existence of temperature field significantly decelerates the speed of domain formation, an effect that has also been seen in Fig. 4. (2) Over the period from $t = 4.0$ to $t = 6.0$, the peak of $S(k,t)$ varies only in height but very little in wave number. This phenomenon is usually observed at the initial stage of phase separation, leading us to think that the system has steered to a new SD stage before reaching the finial late time stage. Essentially, during this stage, the dynamics is mainly making the interfaces thinner while the average domain sizes barely change. (3) At the same time, the peak of $S(k,t)$ in the isothermal case is much larger than the one in the thermal case, but the corresponding wave number is much smaller, which means that both the density difference between the two phases and the characteristic domain size are much larger in the isothermal case. These results agree well with Fig. 4.

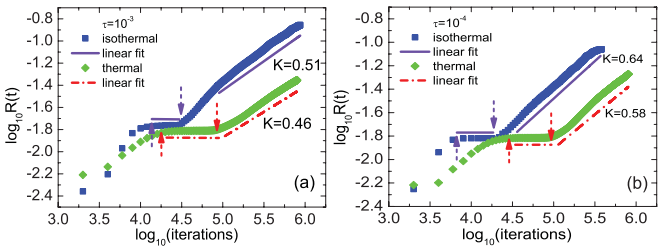

FIG. 6. (Color online) Domain growths in isothermal and thermal systems with (a) $\tau = 10^{-3}$ and (b) $\tau = 10^{-4}$. The squares and diamonds are for results from FFT-TLB simulations. Lines are shown in each plot to guide the eyes.

Next, the characteristic domain size $R(t)$ is used to further describe the kinetic process quantitatively. $R(t)$ is derived from the inverse first moment of $S(k,t)$:

$$R(t) = 2\pi \sum_{k} S(k,t) \Big/ \sum_{k} k S(k,t). \tag{27}$$

In Fig. 6 we display behaviors of $R(t)$ versus iterations for $\tau = 10^{-3}$ in panel (a), and $\tau = 10^{-4}$ in panel (b), in a log-log scale. In each figure the top and bottom scatter symbols correspond to simulation results for the isothermal and thermal cases, respectively. Straight lines in each plot are linear fits of the simulation results. Discarding both the early time transient regime and the very late time regime, where finite-size effects are pronounced, we find, for the isothermal case, the behaviors of $R(t)$ during the DG stage are $R(t) \sim t^{0.52}$ for $\tau = 10^{-3}$, and $R(t) \sim t^{0.64}$ for $\tau = 10^{-4}$. These results are in good agreement with the generally accepted theoretical predictions of $R(t) \sim t^{1/2}$ and $R(t) \sim t^{2/3}$ at high and low viscosities by the Allen-Cahn theory [74] and LB models [28,65,66,69]. But for the thermal case, the growth exponents decrease to 0.46 for $\tau = 10^{-3}$ and 0.58 for $\tau = 10^{-4}$, respectively. This can be regarded as another proof for our conclusion, which states that domains grow faster at lower temperature. In addition to the above differences, another piece of information also deserves our attention. For the isothermal case with $\tau = 10^{-3}$, the SD stage lasts about for 25 000 time steps [see the upper horizontal solid line in Fig. 6(a)]. Nevertheless, for the thermal case, it lasts for 80 000 time steps [see the lower horizontal dash dot line in Fig. 6(a)]. Similar results can also be found in the case with $\tau = 10^{-4}$. These findings suggest that, compared to the isothermal case, the SD stage is significantly prolonged by the existence of the temperature field in the thermal case. In the following parts, the morphological functionals are used to

verify similarities and differences between these two cases, and the corresponding physical interpretations are given.

C. Morphological characterization and physical interpretations

1. Similarities and differences

To perform Minkowski functional analysis for the density map, we choose a density threshold ρ_{th} and pixelize the map into high-density regions (with $\rho > \rho_{\text{th}}$) and low-density regions (with $\rho < \rho_{\text{th}}$). Figure 7 depicts the time evolution of Minkowski measures for the procedures shown in Fig. 4. For the isothermal case, from Fig. 7I(a), we see that, when $\rho_{\text{th}} = 0.40$, the white area fraction A keeps nearly 1.0 during the whole procedure shown here, which means no local density is lower than 0.40 in the system up to $t = 8.0$. However, when the threshold increases to 1.70, A keeps nearly zero during the whole process. Thus, no local density is higher than 1.70 in the system. As a direct consequence of SD, A increases with time t when $\rho_{\text{th}} > 1.0$, and decreases when $\rho_{\text{th}} < 1.0$. Consequently, most curves (except for the uppermost curve for $\rho_{\text{th}} = 0.40$ and the lowermost curve for $\rho_{\text{th}} = 1.70$) are evolving toward the horizontal central line from about $t = 0.25$. Afterwards, at the DG stage, the curve for $\rho_{\text{th}} = 1.05$ (mean density of the system) overlaps with the horizontal central line, and other curves are symmetric to it. The outer two curves are for the cases with $\rho_{\text{th}} = 0.45$ (the red ball) and $\rho_{\text{th}} = 1.60$ (the dark yellow hexagon), respectively. We mention that these two densities are just the equilibrium densities of vapor and liquid at $T = 0.9$. Obviously, the outer two curves mark the reach of the correct equilibrium state. As time evolves further, the proportion between these two curves decreases, showing that these small domains reach local equilibrium. Moreover, the proportion between any two curves can be conveniently obtained from Fig. 7I(a).

Now we go to the second and the third Minkowski measures, the boundary length L and Euler characteristic χ. As shown in Fig. 7I(b), for each case, L increases sharply to its maximum at about $t = 0.25$, and then decreases slowly. The first increase and the subsequent decrease in L are due to the appearance of liquid-vapor interfaces during the SD stage and the following coarsening of the high- and low-density domains during the DG stage, respectively. At the SD stage, when $\rho_{\text{th}} < 1.0$, χ decreases to be evidently less than zero, meaning that the number of domains with $\rho < \rho_{\text{th}}$ increases. On the other hand, when $\rho_{\text{th}} > 1.0$, χ increases to be evidently larger than zero, indicating that the number of domains with $\rho > \rho_{\text{th}}$ increases. These results demonstrate that the phase separation process is in progress. Furthermore, we mention that, at about $t = 0.25$, the case with $\rho_{\text{th}} = 0.45$ has the minimum Euler characteristic and the case with $\rho_{\text{th}} = 1.60$ has the maximum one, but the two cases get the minimum boundary length L. These results present the following information: For the first case, many scattered black domains with $\rho_{\text{th}} < 0.45$ appear in the high-density background with $\rho_{\text{th}} > 0.45$, while for the second case, the high-density domains with $\rho_{\text{th}} > 1.60$ are scattered in the low-density background with $\rho_{\text{th}} < 1.60$. These domains are so small that the total boundary length is nearly zero. From Figs. 4I(c)–4I(d), we observe that the density maps show highly connected structures with nearly equal and very small numbers of black and white domains. Hence, the

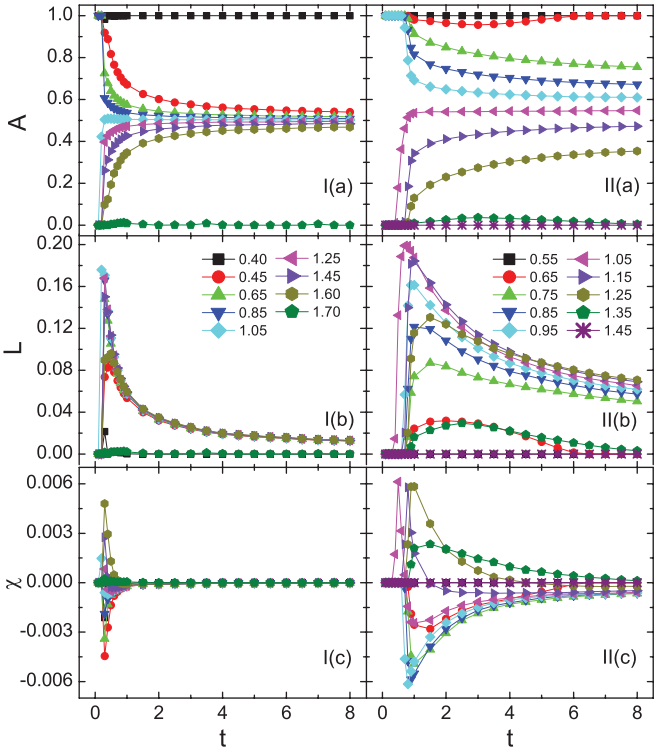

FIG. 7. (Color online) Time evolution of Minkowski measures for the procedures shown in Fig. 4. The left column is for the isothermal case, and the right column is for the thermal case.

Euler characteristic χ keeps close to zero in the DG stage [see Fig. 7I(c)].

From Figs. 7II(a)–II(c), for the thermal case, one can also distinguish two different stages. At early times ($t < 0.8$), due to the growth of density fluctuations and the buildup of interfaces, the density area fraction A belonging to the liquid phase increases, while the one belonging to the vapor phase decreases. The changes also result in the increase in boundary length L [see Fig. 7II(b)]. The appearance of liquid-vapor interfaces has an additional effect. They separate the system with disconnected minority domains. As a result, the absolute value of Euler characteristic χ increases in the SD stage. In contrast to the first stage, as a direct consequence of the coalescence of relatively small domains, the characteristic length scale increases but the number of domains decreases. Therefore, the DG stage ($t > 0.8$) is characterized by the decrease in L and χ.

In the end of the second stage, an interesting phenomenon occurs. There are two small proportions for $\rho < 0.65$ and $\rho > 1.35$ during the second stage, and they reach their maxima at about $t = 3.0$ [see Fig. 7II(a)], but are gradually diminishing afterwards. This phenomenon shows that a recombination process is taking place owing to the increasing temperature that interrupts the original process and forces the system to evolve toward a new equilibrium state decided by the variable temperature.

Compared with figures illustrated in Fig. 7, the main differences between these two cases are analyzed and listed as follows: (1) For isothermal case, the portion with a density between [0.45,1.60] accounts for only 20% at $t = 4$, and

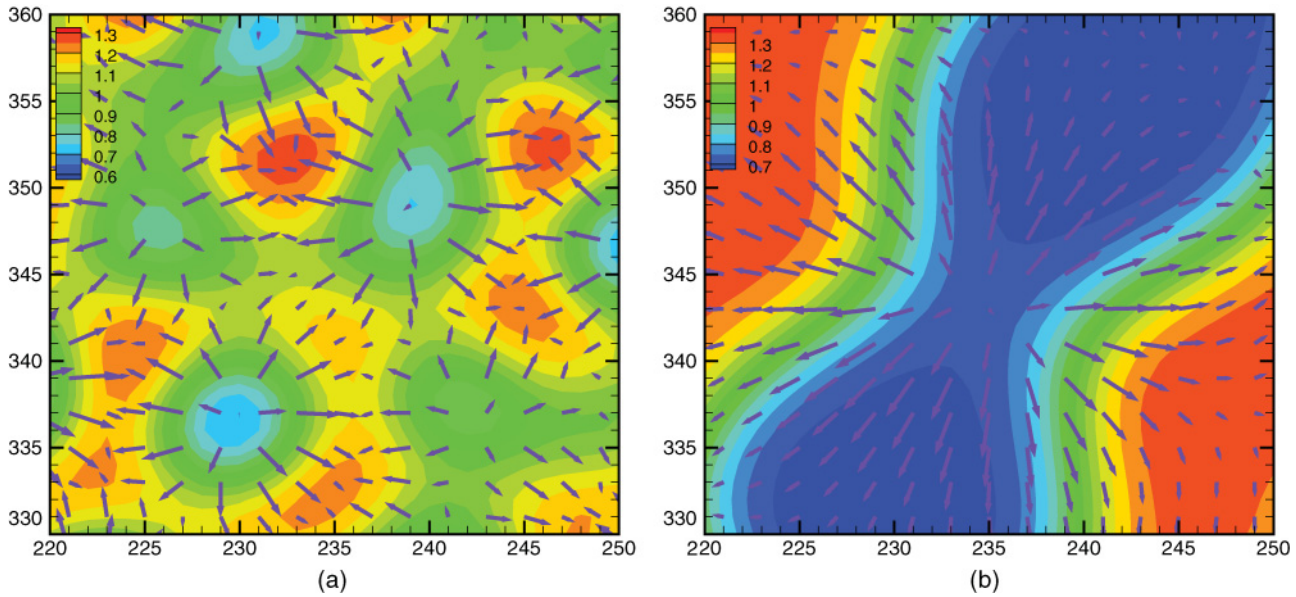

FIG. 8. (Color online) Portions of the density and temperature gradient distributions at (a) $t = 0.8$ and (b) $t = 7.0$ for the thermal case with $\tau = 10^{-3}$. The lengths of the temperature gradient vectors are magnified by (a) 400 times and (b) 4000 times.

decreases further with time t. But for the thermal case, the portion with a density between [0.75,1.25] reaches to 50% at $t = 8$. This indicates that for the thermal case the system has a shallower separation depth but a wider interface width, which can be clearly seen in Fig. 7II(b). (2) The maxima of L and χ can be used to mark the transition from the SD stage to DG stage [27,52]. The transition time for the isothermal case is about 0.25, but for the thermal case, it drastically increases to about 0.8. The result further confirms our conclusion: i.e., phase separation occurs faster in the isothermal case. From another point of view, this can also be obtained from the slope of the $A(t)$ curve. For most cases, after the initial quick changing period, the changing of A with time t shows a slowing down. The slope of the $A(t)$ curve corresponds approximately to the speed of phase separation. For the same density threshold, the slopes of the $A(t)$ curves in the two cases are quite different. For example, when $\rho_{\text{th}} = 0.65$, the $A(t)$ curve decreases sharply in the isothermal case, while for the thermal case, it decreases much more slowly. (3) Connectivity of patterns in the isothermal case is much better than that in the thermal case. This feature can be achieved from the evolution of χ. χ decreases enormously and almost vanishes at about $t = 0.5$ in the isothermal case, but it is negative for the vapor structure until about $t = 6.0$ in the thermal case, which is consistent with density patterns exhibited in Fig. 4II(d).

2. Physical interpretations of the prolonged SD stage and the lower growth exponent in the thermal case: Effects of temperature and viscosity

In Sec. IV, we find, compared to the isothermal case, the SD stage is significantly prolonged, and the growth exponent is lowered in the thermal case. In this subsection, effects of temperature and viscosity are investigated to provide proper interpretations.

First, in Fig. 8, we display portions of the density and temperature gradient distributions at two representative times for the thermal case with $\tau = 10^{-3}$. To illustrate the structure of the temperature gradient fields clearly, the lengths of the vectors are multiplied by 400 in Fig. 8(a) and 4000 in Fig. 8(b), respectively. As shown in Fig. 8(a), many tiny droplets and bubbles appear in the system, and the temperature gradient vectors are toward the droplets. Thus, the local temperatures within droplets are slightly higher than the mean temperature of the system, while the local temperatures within bubbles are slightly lower than the mean temperature. With the separating process, the local temperatures in the two phases deviate more from the mean temperature, and an overshoot phenomenon is observed. This procedure continues up to an extent, after which the local phases with high (low) temperatures partly begin to transform back from liquid (vapor) to vapor (liquid). In this way, both the local high temperatures and low temperatures approach the mean temperature, and the system approaches thermodynamical equilibrium quickly at lower Pr number (Pr = 0.1 for $\tau = 10^{-3}$). This process is evident by Fig. 8(b), where there is no determinate relationship between temperature gradients and liquid (vapor) domains. Moreover, the temperature difference between the highest and lowest ones decreases enormously to 0.014. The system approaches to thermodynamical equilibrium so quickly that the temperature difference becomes so small during phase separation. Therefore, in this case, temperature cannot be regarded as an ideal physical quantity to describe this process.

In another way, we employ enthalpy and latent heat to describe this process, and the enthalpy is defined by

$$h = \epsilon + P/\rho, \tag{28}$$

where $\epsilon = \rho T - 9/8\rho^2 + K|\nabla\rho|^2/2$ is the internal energy density including the gradient contribution. The difference of

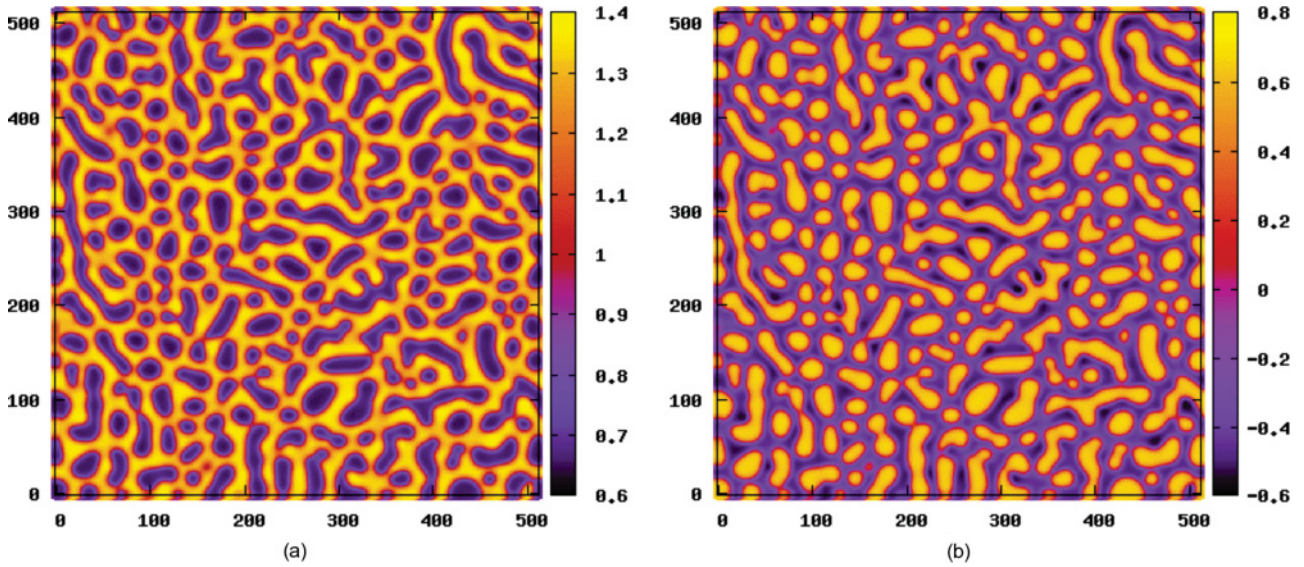

FIG. 9. (Color online) Density (a) and enthalpy (b) distributions at $t = 6.0$ for the thermal case with $\tau = 10^{-3}$.

enthalpy between two states determines the latent heat L_h:

$$L_h = h_2 - h_1. \tag{29}$$

Figure 9 presents the density and enthalpy distributions at $t = 6.0$ for the thermal case with $\tau = 10^{-3}$. Comparisons of the two figures manifest that the enthalpy of vapor is relatively higher than that of liquid. In order to study the dynamic characteristics of the pattern, we show the spatial distribution of latent heat $L_h = h_{t=8.0} - h_{t=3.0}$ in Fig. 10(a) and density change $\Delta\rho = \rho_{t=8.0} - \rho_{t=3.0}$ between these two states in Fig. 10(b). Careful observations between these two figures suggest that when the latent heat L_h is positive, the corresponding density difference $\Delta\rho$ is negative. Droplets (bubbles) absorb latent heat, and evaporation occurs simultaneously. Subsequently, the density decreases. A negative L_h corresponds to an increase of density, and then the droplets (bubbles) have a coagulation trend. It should be noted that, owing to the transformation of potential energy into thermal energy, the total latent heat is released during the whole process. The released heat conducts over the entire region rapidly at low Pr number and increases the mean temperature of the system (see Fig. 11), while in an isothermal system, latent heat is extracted from this system by fixing the temperature in all lattice nodes.

As well, another piece of information can be obtained from Fig. 11. The mean temperature scarcely increases at the first stage due to no detectable phase separation taking place and no remarkable latent heat is released. Subsequently, in the next stage, the temperature rapidly increases to 0.97 and, later, keeps almost zero growth. Afterwards, under the almost unchanged temperature, phase separation evolves in accord with the isothermal case.

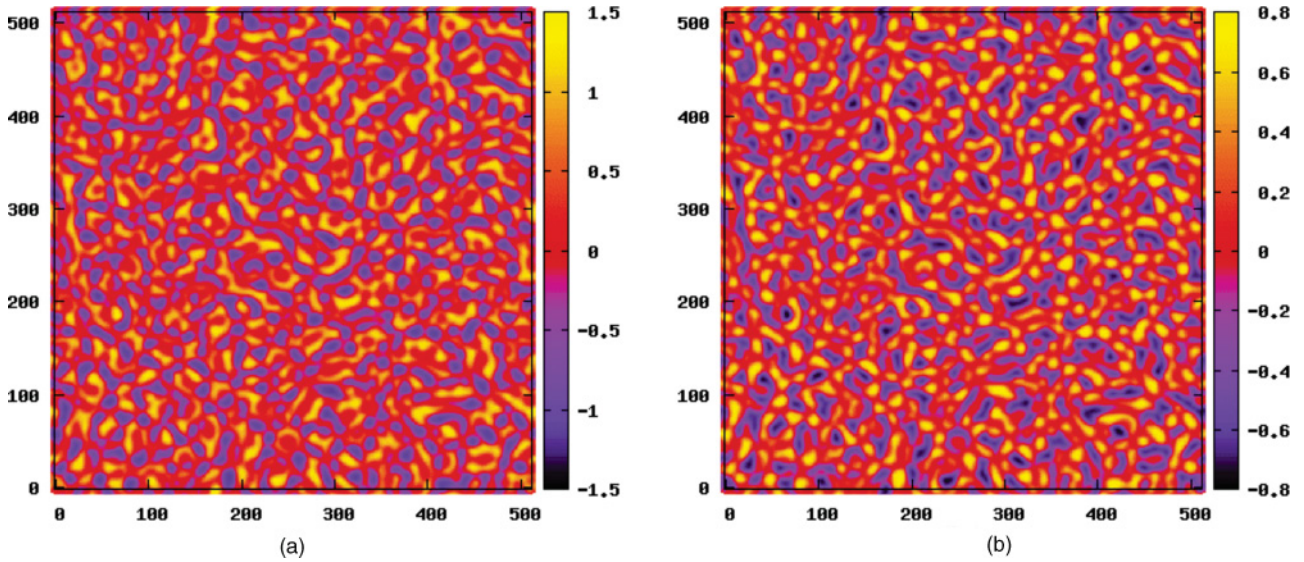

FIG. 10. (Color online) Distribution of latent heat (a) $L_h = h_{t=8.0} - h_{t=3.0}$ and the corresponding distribution of density change (b) $\Delta\rho = \rho_{t=8.0} - \rho_{t=3.0}$ for the thermal case with $\tau = 10^{-3}$.

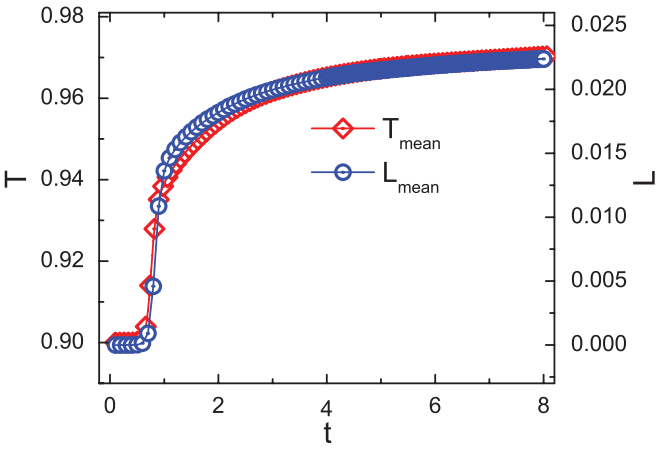

FIG. 11. (Color online) Time evolution of the mean temperature and released latent heat for the procedure shown in panels 4 II(a)–II(d).

So far, we have not discussed in detail surface tension between liquid and vapor. For a planar interface, it can be computed from the following formula [75–77]:

$$\sigma = K \int_{-\infty}^{\infty} \left(\frac{\partial \rho}{\partial z}\right)^2 dz, \tag{30}$$

or from the VDW theory [78–80]:

$$\sigma = \frac{(aK)^{1/2}}{b^2}\sigma^* = \frac{(2aK)^{1/2}}{b^2}\int_{\rho_g^*}^{\rho_l^*} [\Phi^*(\rho^*) - \Phi^*(\rho_l^*)]^{1/2}\, d\rho^*, \tag{31}$$

where

$$\Phi^* = \rho^*\xi - \rho^* T^*[\ln(1/\rho^* - 1) + 1] - \rho^{*2}, \tag{32}$$

$$\xi = T^* \ln(1/\rho_s^* - 1) - \rho_s^* T^*/(1 - \rho_s^*) + 2\rho_s^*, s = v, l. \tag{33}$$

$\rho^* = \rho b$, $T^* = bT/a$, with $a = 9/8$ and $b = 1/3$ in this model. It is necessary to point out that Eq. (31) is especially convenient, since it can be evaluated directly without determining the density profile. Now, we calculate surface tension with Eq. (30) for both the isothermal and thermal cases from profiles along the x axis and, at the same time, calculate theoretical values from Eq. (31). These results are plotted in Fig. 12. It is to be seen that, in the isothermal case, after the formation of liquid-vapor interface, the surface tension σ keeps nearly constant and oscillates slightly around the exact value, while in the thermal case, σ is much smaller than the theoretical value before interfaces are well formed (before the mean temperature reaches 0.96). After that, it decreases obviously with the increase of temperature and can be verified in the following form:

$$\sigma = \sigma_{0.9}[(T_c - T)/(T_c - 0.9)]^{3/2}, \tag{34}$$

where $\sigma_{0.9}$ is the surface tension at $T = 0.9$. The increasing temperature lowers the density gradient, as well as the surface tension that is the driving force for diffusive growth. As a result, domains grow more slowly than that in the isothermal case.

Essentially, during the whole process, compared to the isothermal case, two competition mechanisms exist. The first

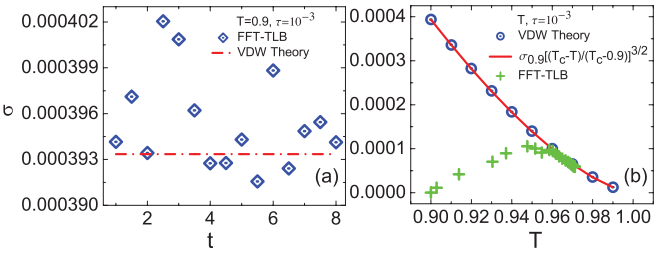

FIG. 12. (Color online) Time evolution of surface tension for the procedures shown in Fig. 4. (a) The isothermal case; (b) the thermal case.

one is heat generation and conduction mechanism or temperature rising mechanism. The release of latent heat results in a rising temperature, and the rising temperature results in a new dependence of pressure density [38,39]. In other words, it leads to a new local mechanical balance. The second one is the hydrodynamic flow generation and development mechanism, or liquid-vapor equilibrium mechanism, decided by viscosity, diffusivity of the fluid, etc. They compete with and influence each other, deciding the final morphology jointly.

In addition to the temperature effects, we now consider how the local viscosities influence the hydrodynamic flows, the morphology of the phase-separating system, and the growth exponent. Figure 13 shows time evolution of the high-velocity $|\mathbf{u}|$ area fraction for the procedures displayed in Fig. 4. From it, also, two stages can be found, corresponding to the nearly zero value of the white area fraction for all $|\mathbf{u}|_{\text{th}}$, the rapid increase and the subsequent slow decrease. For the isothermal case, $|\mathbf{u}| \in [0,0.09]$, while for the thermal case, $|\mathbf{u}| \in [0,0.02]$. This implies that velocities are damped not only by viscosity but also by the rising temperature. In fact, this is owing to the latent heat released or absorbed at the interface that makes temperatures within bubbles (droplets) almost homogeneous [38,39], as shown in Fig. 8(b). As a result, the Marangoni convection arising from the surface tension gradient is much suppressed. The maximum velocity in the isothermal case can reach up to 0.09 or even higher. Consequently, in contrast to the thermal case, hydrodynamic effects can not be totally neglected in the isothermal case. The appearance of larger flow velocities offers more opportunities for coalescence between domains. Under the action of diffusion and hydrodynamic flows, a faster DG process is taking place, and a bigger growth exponent can be observed. When τ decreases to 10^{-4},

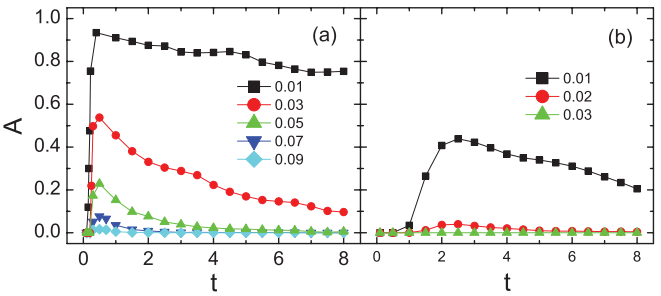

FIG. 13. (Color online) High flow velocity area fraction A versus time t for the procedures shown in Fig. 4. (a) The isothermal case; (b) the thermal case.

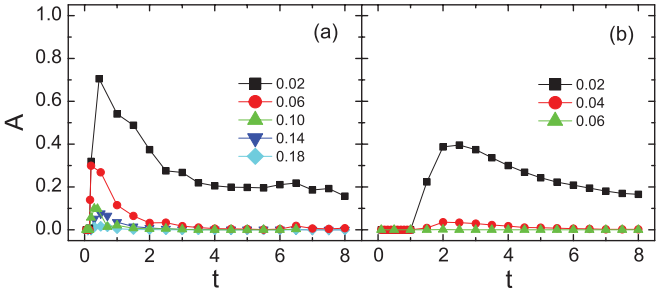

FIG. 14. (Color online) High flow velocity area fraction A versus time t for two phase separation procedures with $\tau = 10^{-4}$. (a) The isothermal case; (b) the thermal case.

behaviors of $|\mathbf{u}|$ exhibit similar trends (see Fig. 14). Due to the lower viscosity, velocities are more sufficiently developed. Figures 13 and 14 demonstrate that, in the thermal case, compared to the thermodynamic and diffusion mechanisms, hydrodynamic flows are less important than that in the isothermal case and, therefore, cannot be regarded as a dominant factor governing the growth exponent.

In Fig. 15 we display time evolution of each part of total energy for the procedure shown in Figs. 4II(a)–II(d), providing a clear image about energy evolution during phase separation. It is found that ρT and $-9\rho^2/8$ are the main parts of total energy, and they evolve in the opposite way. Kinetic energy and surface energy are much smaller than the two former ones. The maximum of $K|\nabla\rho|^2/2$ corresponds to the appearance of nuclei and formation of small domains. Afterwards, it decreases gradually due to the increasing temperature and the decreasing interfacial area. The macroscopic kinetic energy $\rho u^2/2$ is so small that the viscous dissipation induced by it can be neglected. Therefore, in the thermal case, compared to latent heat, the effects of kinetic energy on temperature are less important.

V. CONCLUSIONS AND DISCUSSIONS

Thermal and isothermal symmetric liquid-vapor separations are simulated via the FFT-TLB method. Structure factor, domain size, and Minkowski functionals are used to describe the density and velocity fields and, at the same time, to understand the configurations and the kinetic processes. Simulations and physical analysis present the following scenarios for thermal phase separation. When the separation starts, many tiny droplets and bubbles appear in the system. The

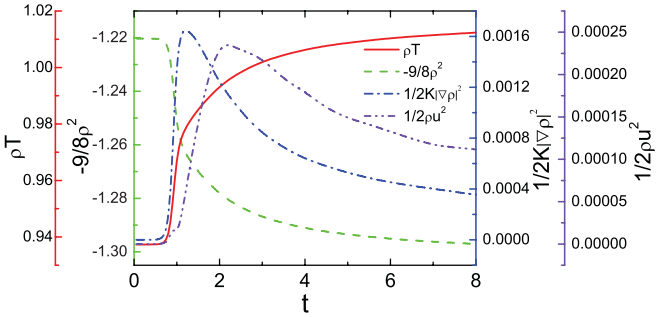

FIG. 15. (Color online) Time evolution of each part of total energy for the procedure shown in panels 4II(a)–II(d).

local temperatures within droplets are slightly higher than the ones within bubbles. With separating, neighboring droplets (bubbles) coalesce, and the mean domain size increases. The local temperatures in the two phases deviate more from the mean temperature. This procedure continues up to a stage, after which the local phases with high (low) temperatures partly begin to transform back from liquid (vapor) to vapor (liquid). In this way, both the local high temperatures and low temperatures approach the mean one, and the system approaches thermodynamical equilibrium.

Simulation results also indicate that phase separation in the thermal and isothermal cases can be generally divided into two stages: the SD stage and the DG stage. Different from the isothermal case, the SD stage is significantly prolonged, and different rheological and morphological behaviors are induced by the variable temperature field in the thermal case. After the transient procedure, both the thermal and isothermal separations show power-law scalings in the domain growth, while the exponent for thermal system is lower than that for isothermal system. With respect to the density field, the isothermal system presents more likely bicontinuous configurations with narrower interfaces, while the thermal system presents more likely configurations with scattered bubbles.

Compared with the isothermal case, heat creation, conduction, and lower interfacial stresses are the main reasons for the differences in thermal system. Latent heat is released during the separating process, which is the main reason for the rising temperature. The changing of local temperature results in new local mechanical balance. When the Prandtl number becomes smaller, the system approaches thermodynamical equilibrium more quickly. The increasing local temperature has an additional effect: It makes the interfacial stress lower. This behavior in simulations is quantitatively verified by the theoretical formula, $\sigma = \sigma_0[(T_c - T)/(T_c - T_0)]^{3/2}$, where T_c is the critical temperature and σ_0 is the interfacial stress at a reference temperature T_0. Besides thermodynamics, we find that the local viscosities also influence the morphology of the phase separating system. For both the isothermal and thermal cases, growth exponents and local flow velocities are inversely proportional to the corresponding viscosities. Compared with the isothermal case, the local flow velocities in the thermal case depend not only on viscosity but also on temperature.

The FFT scheme can also be applied in systems that have walls in the x and/or y directions [36,37,45,70] provided that the following simple treatments are made. For example, for a system with left and right walls, we can simply double the computational domain by making a mirror reflection of the original one around the right (or left) wall. Thus, for the extended computational domain, the left and the right walls are exactly the same. We can consider the system periodic, and the FFT scheme can be used in the horizontal direction. In future studies, we will increase the depth of separation that the FFT-TLB model can undergo, and investigate quantitatively how the Prandtl number affects the separation procedure.

ACKNOWLEDGMENTS

The authors sincerely thank the anonymous reviewers for their valuable comments and suggestions, which were

very helpful for revising the manuscript. Also, we warmly thank Dr. Victor Sofonea and Dr. G. Gonnella for many instructive discussions, suggestions, and encouragement, and Prof. Jianhua Wei, Dr. Qinli Zhang, and Dr. Bohai Chen for many useful suggestions. AX and GZ acknowledge support of the Science Foundations of LCP and CAEP (under Grant Nos. 2009A0102005 and 2011A0201002) and the National Natural Science Foundation of China (under Grant Nos. 11075021 and 11074303). YG and YL acknowledge support of the National Basic Research Program (973 Program) (under Grant No. 2007CB815105), National Natural Science Foundation of China (under Grant No. 11074300), Fundamental Research Funds for the Central University (under Grant No. 2010YS03), Technology Support Program of LangFang (under Grant Nos. 2010011029/30/31), and Science Foundation of NCIAE (under Grant Nos. 2008-KY-13 and KY-2010-06).

[1] C. Brennen, *Fundamentals of Multiphase Flow* (Cambridge University Press, Cambridge, 2005).
[2] V. Starikovicius, Berichte des Fraunhofer ITWM, Nr **55** (2003).
[3] R. Held and M. Celia, Adv. Water Resour. **24**, 325 (2001).
[4] J. Horbach and S. Succi, Phys. Rev. Lett. **96**, 224503 (2006).
[5] Z. Guo and T. S. Zhao, Phys. Rev. E **68**, 035302(R) (2003).
[6] S. Succi, *The Lattice Boltzmann Equation for Fluid Dynamics and Beyond* (Oxford University Press, New York, 2001).
[7] S. Succi, M. Vergassola, and R. Benzi, Phys. Rev. A **43**, 4521 (1991).
[8] V. Sofonea and W. Früh, Eur. Phys. J. B **20**, 141 (2001).
[9] M. Watari and M. Tsutahara, Phys. Rev. E **67**, 036306 (2003).
[10] A. Xu, Phys. Rev. E **71**, 066706 (2005); Europhys. Lett. **71**, 651 (2005).
[11] Y. Gan, A. Xu, G. Zhang, X. Yu, and Y. Li, Physica A **387**, 1721 (2008).
[12] F. Chen, A. Xu, G. Zhang, Y. Li, and S. Succi, Europhys. Lett. **90**, 54003 (2010); F. Chen, A. Xu, G. Zhang, and Y. Li, Phys. Lett. A **375**, 2129 (2011).
[13] J. Zhang, G. Yan, and X. Shi, Phys. Rev. E **80**, 026706 (2009).
[14] X. He, S. Chen, and R. Zhang, J. Comput. Phys. **152**, 642 (1999).
[15] Y. Gan, A. Xu, G. Zhang, and Y. Li, Phys. Rev. E **83**, 056704 (2011).
[16] A. K. Gunstensen, D. H. Rothman, S. Zaleski, and G. Zanetti, Phys. Rev. A **43**, 4320 (1991).
[17] X. Shan and H. Chen, Phys. Rev. E **47**, 1815 (1993); **49**, 2941 (1994).
[18] M. R. Swift, W. R. Osborn, and J. M. Yeomans, Phys. Rev. Lett. **75**, 830 (1995); G. Gonnella, E. Orlandini, and J. M. Yeomans, *ibid*. **78**, 1695 (1997); A. J. Wagner and J. M. Yeomans, *ibid*. **80**, 1429 (1998); D. Marenduzzo, E. Orlandini, and J. M. Yeomans, *ibid*. **92**, 188301 (2004).
[19] A. J. Briant, A. J. Wagner, and J. M. Yeomans, Phys. Rev. E **69**, 031602 (2004).
[20] H. Huang, D. T. Thorne, M. G. Schaap, and M. C. Sukop, Phys. Rev. E **76**, 066701 (2007).
[21] J. Hyväuoma, P. Raiskinmäi, A. Jäberg, A. Koponen, M. Kataja, and J. Timonen, Phys. Rev. E **73**, 036705 (2006); J. Hyväuoma, T. Turpeinen, P. Raiskinmäi, A. Jäberg, A. Koponen, M. Kataja, J. Timonen, and S. Ramaswamy, *ibid*. **75**, 036301 (2007).
[22] H. Xi and C. Duncan, Phys. Rev. E **59**, 3022 (1999).
[23] A. N. Kalarakis, V. N. Burganos, and A. C. Payatakes, Phys. Rev. E **65**, 056702 (2002).
[24] K. N. Premnath and J. Abraham, Phys. Rev. E **71**, 056706 (2005); Phys. Fluids **17**, 122105 (2005).
[25] K. Furtado and J. M. Yeomans, Phys. Rev. E **73**, 066124 (2006).
[26] A. Xu, G. Gonnella, and A. Lamura, Phys. Rev. E **67**, 056105 (2003); **74**, 011505 (2006); Physica A **331**, 10 (2004); **344**, 750 (2004); **362**, 42 (2006); A. Xu, G. Gonnella, A. Lamura, G. Amati, and F. Massaioli, Europhys. Lett. **71**, 651 (2005).
[27] V. Sofonea and K. Mecke, Eur. Phys. J. B **8**, 99 (1999).
[28] V. Sofonea, A. Lamura, G. Gonnella, and A. Cristea, Phys. Rev. E **70**, 046702 (2004); A. Cristea, G. Gonnella, A. Lamura, and V. Sofonea, Commun. Comput. Phys. **7**, 350 (2010).
[29] X. He and G. Doolen, J. Stat. Phys. **107**, 309 (2002).
[30] X. Shan, Phys. Rev. E **73**, 047701 (2006).
[31] P. Yuan and L. Schaefer, Phys. Fluids **18**, 042101 (2006).
[32] T. Lee and P. F. Fischer, Phys. Rev. E **74**, 046709 (2006).
[33] T. Seta and K. Okui, J. Fluid Sci. Technol. **2**, 139 (2007).
[34] M. Sbragaglia, R. Benzi, L. Biferale, X. Shan, H. Chen, and S. Succi, J. Fluid Mech. **628**, 299 (2009).
[35] A. Tiribocchi, N. Stella, G. Gonnella, and A. Lamura, Phys. Rev. E **80**, 026701 (2009).
[36] G. Gonnella, A. Lamura, A. Piscitelli, and A. Tiribocchi, Phys. Rev. E **82**, 046302 (2010).
[37] G. Gonnella, A. Lamura, and A. Tiribocchi, Philos. Trans. R. Soc. London A **369**, 2592 (2011).
[38] A. Onuki, *Phase Transition Dynamics* (Cambridge University Press, Cambridge, UK, 2002).
[39] A. Onuki, Phys. Rev. Lett. **94**, 054501 (2005); Phys. Rev. E **75**, 036304 (2007); A. Onuki and K. Kanatani, *ibid*. **72**, 066304 (2005); R. Teshigawara and A. Onuki, Europhys. Lett. **84**, 36003 (2008); Phys. Rev. E **82**, 021603 (2010).
[40] R. Zhang and H. Chen, Phys. Rev. E **67**, 066711 (2003).
[41] P. Yuan, Ph.D. thesis, University of Pittsburgh, 2005.
[42] F. J. Alexander, S. Chen, and J. D. Sterling, Phys. Rev. E **47**, R2249 (1993).
[43] X. Shan, X. Yuan, and H. Chen, J. Fluid Mech. **550**, 413 (2006).
[44] P. C. Philippi, L. A. Hegele, L. O. E. dos Santos, and R. Surmas, Phys. Rev. E **73**, 056702 (2006); D. Siebert, L. Hegele, R. Surmas, L. Santos, and P. Philippi, Int. J. Mod. Phys. C **18**, 546 (2007); R. Surmas, C. PicoOrtiz, and P. Philippi, Eur. Phys. J. Spec. Top. **171**, 81 (2009).
[45] G. Gonnella, A. Lamura, and V. Sofonea, Phys. Rev. E **76**, 036703 (2007).
[46] Y. Gan, A. Xu, G. Zhang, and Y. Li, e-print arXiv:1011.3582v3.
[47] H. Minkowski, Math. Ann. **57**, 447 (1903).
[48] A. Rosenfeld and A. Kak, *Digital Picture Processing* (Academic Press, New York, 1976).
[49] K. R. Mecke, Phys. Rev. E **53**, 4794 (1996).
[50] A. Xu, G. Zhang, X. Pan, P. Zhang, and J. Zhu, J. Phys. D **42**, 075409 (2009); A. Xu, G. Zhang, Y. Ying, P. Zhang, and J. Zhu, Phys. Scri. **81**, 055805 (2010).

[51] A. Aksimentiev, K. Moorthi, and R. Holyst, J. Chem. Phys. **112**, 1 (2000).
[52] K. R. Mecke and V. Sofonea, Phys. Rev. E **56**, R3761 (1997).
[53] H. Hadwiger, Math. Z. **71**, 124 (1959).
[54] H. Zhang and M. Shen, *Computational Fluid Dynamics: Fundamentals and Applications of Finite Difference Methods* (National Defense Industry Press, Beijing, 2003) (in Chinese).
[55] G. Jiang and C. Shu, J. Comput. Phys. **126**, 202 (1996).
[56] K. Liang, *Methods of Mathematical Physics* (Higher Education Press, Beijing, 1998) (in Chinese).
[57] C. Canuto, M. Hussaini, A. Quarteroni, and T. Zang, *Spectral Methods in Fluid Dynamics* (Springer, London, 1987).
[58] C. Birdsall and A. Langdon, *Plasma Physics via Computer Simulation* (Adam Hilger, Bristol, 1991).
[59] J. Boyd, *Chebyshev and Fourier Spectral Methods* (Dover Publications, New York, 2000).
[60] S. Orszag, Phys. Rev. Lett. **26**, 1100 (1971).
[61] M. Hussaini, D. Kopriva, M. Salas, and T. Zang, AIAA J. **23**, 64 (1985).
[62] Y. Sun, Y. Zhou, S. Li, and G. Wei, J. Comput. Phys. **214**, 466 (2006).
[63] C. Shu, NASA/CR-97-206253 ICASE Report No. 97-65 (1997).
[64] A. Bray, Adv. Phys. **43**, 357 (1994).
[65] F. J. Alexander, S. Chen, and D. W. Grunau, Phys. Rev. B **48**, 634 (1993).
[66] W. R. Osborn, E. Orlandini, M. R. Swift, J. M. Yeomans, and J. R. Banavar, Phys. Rev. Lett **75**, 4031 (1995).
[67] D. W. Grunau, T. Lookman, S. Y. Chen, and A. S. Lapedes, Phys. Rev. Lett. **71**, 4198 (1993).
[68] S. Chen and T. Lookman, J. Stat. Phys. **81**, 223 (1995).
[69] J. M. Yeomans, Annu. Rev. Comp. Phys. **VII**, 61 (2000).
[70] G. Gonnella1, A. Lamura, and A. Piscitelli, J. Phys. A **41**, 105001 (2008).
[71] A. Lamorgese and R. Mauri, Phys. Fluids **21**, 044107 (2009).
[72] V. M. Kendon, J. C. Desplat, P. Bladon, and M. E. Cates, Phys. Rev. Lett. **83**, 576 (1999).
[73] N. González-Segredo, M. Nekovee, and P. V. Coveney, Phys. Rev. E **67**, 046304 (2003).
[74] S. Allen and J. Cahn, Acta Metall. **27**, 1085 (1979).
[75] J. Rowlinson and B. Widom, *Molecular Theory of Capillarity* (Clarendon Press, Oxford, 1982).
[76] T. Inamuro, N. Konishi, and F. Ogino, Comput. Phys. Commun **129**, 32 (2000).
[77] T. Inamuro, T. Ogata, S. Tajima, and N. Konishi, J. Comput. Phys. **198**, 628 (2004).
[78] V. Bongiorno and H. Davis, Phys. Rev. A **12**, 2213 (1975).
[79] B. F. McCoy and H. T. Davis, Phys. Rev. A **20**, 1201 (1979).
[80] E. S. Kikkinides, A. G. Yiotis, M. E. Kainourgiakis, and A. K. Stubos, Phys. Rev. E **78**, 036702 (2008).